ARTICLE

Connectomic reconstruction of the inner plexiform layer in the mouse retina

Moritz Helmstaedter[1]†, Kevin L. Briggman[1]†, Srinivas C. Turaga[2]†, Viren Jain[2]†, H. Sebastian Seung[2] & Winfried Denk[1]

Comprehensive high-resolution structural maps are central to functional exploration and understanding in biology. For the nervous system, in which high resolution and large spatial extent are both needed, such maps are scarce as they challenge data acquisition and analysis capabilities. Here we present for the mouse inner plexiform layer—the main computational neuropil region in the mammalian retina—the dense reconstruction of 950 neurons and their mutual contacts. This was achieved by applying a combination of crowd-sourced manual annotation and machine-learning-based volume segmentation to serial block-face electron microscopy data. We characterize a new type of retinal bipolar interneuron and show that we can subdivide a known type based on connectivity. Circuit motifs that emerge from our data indicate a functional mechanism for a known cellular response in a ganglion cell that detects localized motion, and predict that another ganglion cell is motion sensitive.

Information about neuronal wiring has long been the basis of formulating and testing ideas about how computation is performed by neural circuits. Complete[1,2] and partial[3–5] wiring diagrams are being used where available. Whether such diagrams can be created by statistical extrapolation or whether higher-order connectivity is functionally important is highly controversial[6–9]. The assumption that mingling neurites connect (Peters' rule[10]) allows connectivity to be inferred from light-microscopic observations of sparsely stained tissue, but is frequently violated[5,7], showing that connectivity must be explicitly tested rather than inferred from proximity. Simultaneous electrical recordings from several cells can determine and quantify their synaptic connectivity[11–13], but do not allow a comprehensive sampling of connections.

Unlike light microscopy, electron microscopy can follow even the thinnest neurites through densely stained neuropil, and can detect unambiguously whether two cells touch and over which area[1,14]. Serial section transmission electron microscopy was, for example, used to reconstruct the complete wiring diagram of the roundworm *Caenorhabditis elegans*[1,2] and to study synaptic connectivity in the retina[15–17]. Volume electron microscopy data sets hundreds of micrometres in extent[18] have been used to reconstruct—guided by previous functional imaging—specific neural circuits[5,18].

The retina performs a variety of image-processing tasks and is one of the best studied parts of the central nervous system[19]. But, only in few cases, such as for direction sensitivity (reviewed in ref. 20), has the underlying neural computation been plausibly explained, combining information from anatomical studies, electrical recordings and two-photon calcium imaging[5,12,20–23].

Here we combined serial block-face electron microscopy (SBEM)[24] data, crowd-sourced manual annotation[25], machine learning-based boundary detection[26,27], and automatic volume segmentation to reconstruct the neurites of 950 neurons in a $114\,\mu m \times 80\,\mu m$ area of the inner plexiform layer (IPL) and all their contacts in that volume.

We establish the validity of the reconstruction using known circuits and demonstrate its use by classifying cells based on their electron-microscopy-resolution morphology, by isolating a new type of bipolar cell, by showing that the cell-to-type contact area is in some cases tightly controlled and can be used to augment type classification, and by uncovering several cases in which neurite co-stratification does not predict a contact. Among the functional implications of these findings is the prediction that a particular ganglion cell is motion sensitive.

Imaging and reconstruction

We used SBEM because a superior z-resolution[18] and lack of image distortions makes SBEM data sets more easily traced by humans[5] and segmented by computers. The main data set used in this study (e2006) has a volume of more than 1 million μm^3, includes all layers that contain intra-retinal synaptic connections, and was stained to enhance plasma-membrane visibility[5], further facilitating traceability and automated segmentation.

Because completely labelling such a volume by hand would be prohibitively expensive (about US$10 million), we tried to establish an entirely automatic reconstruction pipeline. Our SBEM data can be automatically segmented into objects that represent the local cellular geometry acurately[26,27]. But even at voxel error rates of a few per cent, cells get fragmented into many pieces (M.H. *et al.*, manuscript in preparation). Manually traced skeletons, on the other hand, do reliably establish intra-cellular continuity over large distances[25] but allow neither identification nor quantification of cell–cell contacts, and visually inspecting close skeleton encounters[5] is impractical for the large number (roughly 10^6) expected in our data set. Therefore, we separately created skeletons for all cells by crowd-sourced manual annotation, which is much faster than manual volume tracing[25], and volume segmentation (see below).

Skeletons were created by a team of trained human annotators, which included, over time, more than 224 different students. First, the annotators identified all somata and classified them as photoreceptor ($n > 2,000$), glial ($n = 173$), horizontal ($n = 33$), bipolar ($n = 496$), amacrine ($n = 407$) or ganglion ($n = 47$) cells, based on soma location and emerging neurites (Fig. 1a). Starting from the somata, the annotators skeletonized the neurites of all glial, bipolar (Fig. 1b), amacrine and ganglion cells using the KNOSSOS program[25] (http://www.knossostool.org). Multiple tracings by different annotators (average redundancies: 6,

[1]Max-Planck Institute for Medical Research, D-69120 Heidelberg, Germany. [2]Department of Brain and Cognitive Sciences, Howard Hughes Medical Institute, Massachusetts Institute of Technology, Cambridge, Massachusetts 02139, USA. †Present addresses: Max-Planck Institute of Neurobiology, D-82152 Martinsried, Germany (M.H.); National Institute of Neurological Disorders and Stroke, National Institutes of Health, Bethesda, Maryland 20892, USA (K.L.B.); Gatsby Computational Neuroscience Unit, London WC1N 3AR, UK (S.C.T.); Howard Hughes Medical Institute, Janelia Farm Research Campus, Ashburn, Virginia 20147, USA (V.J.).

4 and 4 for ganglion, amacrine and bipolar cells, respectively), were automatically consolidated[25], visually inspected and, in a few cases, manually corrected. A total of >20,000 annotator hours yielded 2.6 m of skeletons, representing 0.64 m of neurite, with estimated[25] error rates of 9, 12 and 6 per ganglion, amacrine and bipolar cell, respectively.

Cell types

We classified all neurons into cell types by visual inspection of the bare skeletons, with a focus on the IPL. We found $n = 459$ almost complete bipolar cells (Fig. 1c; all reconstructed types and cells are shown in Supplementary Data 1 and 6, respectively). Most bipolar cells clearly belonged to one of the 10 types described previously[28] (Fig. 1c). However, particularly for OFF cone bipolar cells (CBCs) (1–4), some classification ambiguity remained, even after taking into account tiling. A random re-examination of 59 ON CBCs (CBC5–9) found one error.

Seven cells showed no similarity to any of the ten bipolar types[28], but shared a distinct morphology and were designated as XBCs (Fig. 1d and Supplementary Data 2a). XBC axons stratify more narrowly but at the same average depth as CBC5 (Fig. 1d, e). Laterally, XBC axons roam widely, similar to CBC9, but their dendrites are comparatively compact, different from CBC9 (Supplementary data 2b), and their depth suggests that they contact cones.

The dendrites of all ganglion cells and of many amacrine cells extended beyond the data set volume. Many ganglion and amacrine cells could nevertheless be grouped by inspecting their neurites (12 ganglion cell types, Fig. 2a, b; 12 narrow-field amacrine cell types, Fig. 2c, d; 33 medium/wide-field amacrine cell types, including 6 displaced types, Fig. 2e, f and Supplementary Data 1 and 6). We used the type-averaged (for individual variations see Supplementary Data 1) neurite density over depth in the IPL (Fig. 2) to create for all amacrine and ganglion cell types unique identifiers (ac64-73, for example, is an amacrine cell type with first and third quartiles at 64% and 73% IPL depth, respectively). Prominent among cell types previously known (see Supplementary Data 7 for a complete listing) are gc30-63, ac25-31 and ac60-65, corresponding to ON/OFF direction-selective ganglion cells[29] (DSGCs; Fig. 2a) and ON and OFF starburst amacrine cells[16] (SACs; Fig. 2e), respectively.

Contact detection

We next combined the skeletons with an automatic segmentation (Fig. 3), created by first training a convolutional network to detect cell boundaries[27], followed by several growth and merge steps (Fig. 3a). The final volume consolidation into a representation of the cellular geometry was performed by combining for each cell all segments overlapping its skeleton (Fig. 3b, typically several hundred segments; total estimated volume error rate about 3%, see Methods).

Of 1,123 fully volume-reconstructed cells, 173 were glia, 110 were orphans (one-of-a-kind cells or cells without a reasonable neurite morphology), and 840 were the neurons used in the analysis. All contacts ($n = 579,724$) between them were automatically detected and quantified (Fig. 3c, Supplementary Data 5 and Methods). When testing
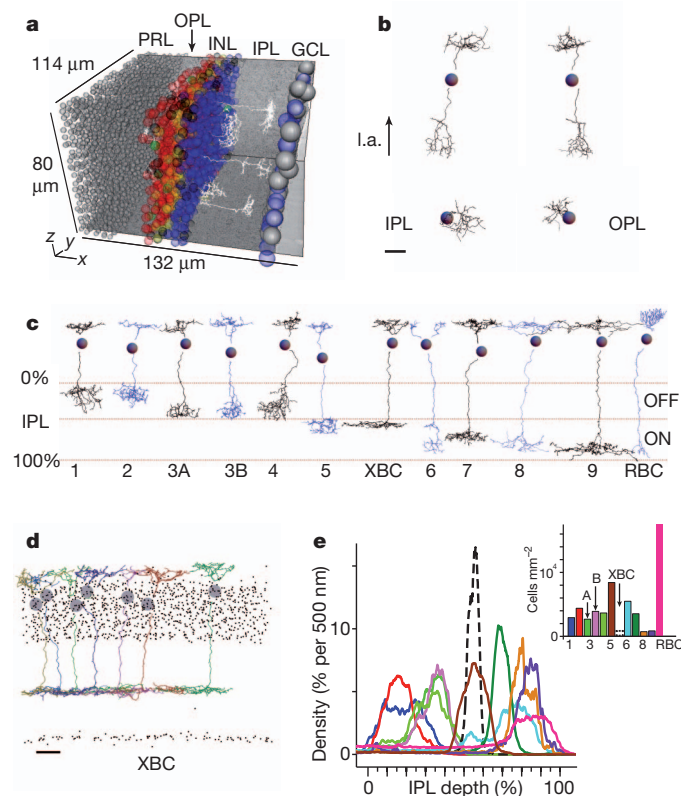
Figure 1 | Raw data, skeletons and bipolar cell analysis. a, Somata, from the left: photoreceptor (grey), horizontal (green), bipolar (red), glia (yellow), amacrine (blue) and ganglion (grey) cells. Also shown (white) are axons for two CBC1, one CBC6 and two CBC7 cells. GCL, ganglion cell layer; INL, inner nuclear layer; OPL, outer plexiform layer; PRL, photoreceptor layer. **b,** Side views from two orthogonal directions onto a single CBC4 skeleton (top), and light-axis (l.a.) views of dendrite (left) and axon (bottom). **c,** One example for each bipolar cell type. **d,** All XBC skeletons, side view. **e,** Skeleton density (segment length/vote count, normalized across IPL) versus depth for all bipolar cell types (one profile shown for the entire CBC5 population). Inset: bipolar cell prevalence (colours as for depth profiles). Scale bars, 10 μm.
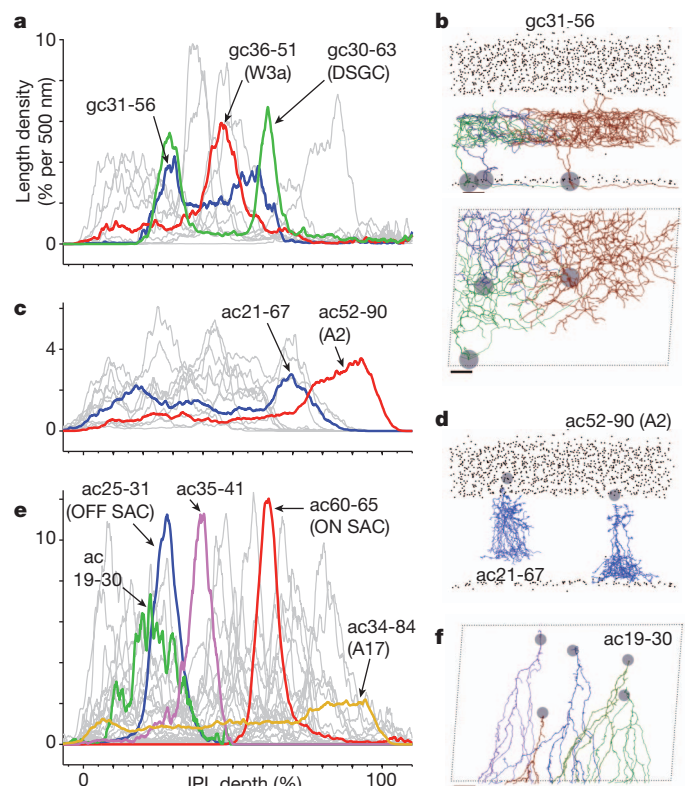
Figure 2 | Ganglion and amacrine cells. a, Normalized ganglion cell depth profiles for gc31-56, gc36-51 (W3), gc30-63 (DSGC) and the remaining cell types (grey). **b,** All three gc31-56 cells (somata: grey disks, side (top) and light-axis (bottom) views), and all other inner nuclear layer and ganglion cell layer (somata: black dots, side view only). **c,** Narrow-field amacrine cell depth profiles for ac21-67, ac52-90 (A2) and remaining narrow-field amacrine cells (grey). **d,** One example each for ac21-67 and ac52-90 (A2). **e,** Medium-field amacrine depth profiles for ac19-30, ac25-31 (OFF SAC), ac35-41, ac60-65 (ON SAC), ac34-84 (A17) and remaining medium-field amacrine cells (grey). **f,** Light-axis view for ac19-30. Scale bars, 10 μm.
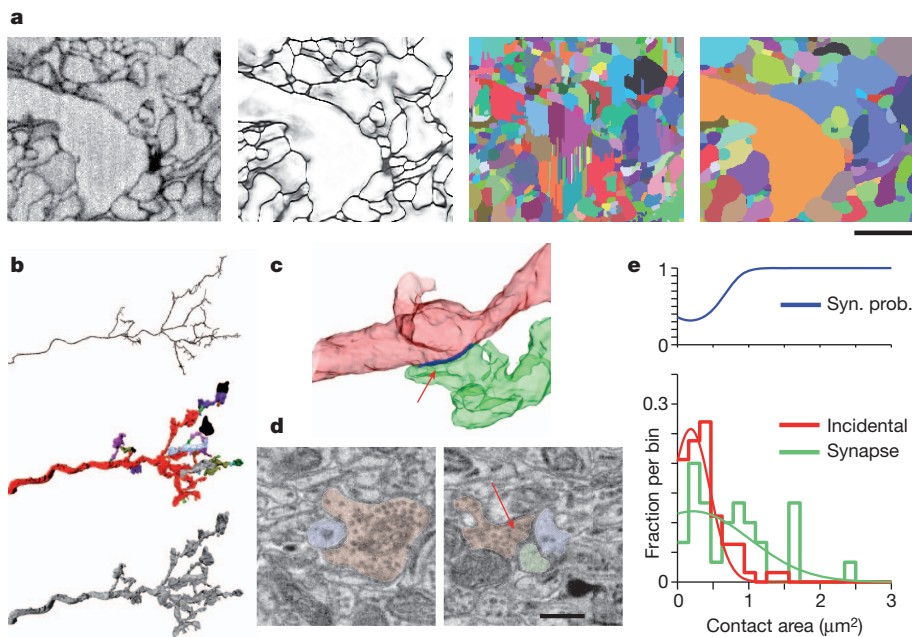
Figure 3 | Automatic segmentation and contact detection. a, From left: raw data (offset and contrast adjusted), edge classifier (*xyz* average), initial and iterated segmentations (see also Supplementary Data 3e–g). **b**, From top: bare skeleton, skeleton with overlapping segmentation objects, and the resulting volume representation for a CBC6 axon. **c**, Automatically detected contact (red arrow) between a CBC5 cell and a DSGC (gc30-63). **d**, Cross-sections through a non-synaptic contact (left, Supplementary Data, 3a, b) and a ribbon synapse (right) from data set k563, coloured by hand. **e**, Frequencies (bottom) of non-synaptic (red, $n = 63$) and synaptic (green, $n = 30$) cell–cell contacts versus contact area and the Gaussian fits to them (thin lines, centre/width: 0.18/0.38 and 0.22/1.13, all in μm^2) and the resulting synapse probability (syn. prob.) estimate (top). Scale bars, 1 μm (**a**), 500 nm (**d**).

the reliability of the algorithm, we found that it missed none of 16 contacts visually identified in the raw data, and 20 randomly selected algorithm-generated contacts contained only one false contact (caused by debris in one image).

The cell-to-cell contact-area matrix (Fig. 4a and Supplementary Data 4) includes only contacts that are individually below 5 μm² (about 99.9% of all contacts), thus excluding touching somata and neurite bundles, and was then condensed into a type-to-type matrix (Fig. 4b and Supplementary Data 4). When exploring the circuit that couples rod photoreceptor signals into the cone pathway[30], we found the A2 amacrine cell (ac52-90) contacting the rod bipolar cell (RBC) very strongly (with 23.6% of the A2 cell total detected neuronal contact area), contacting OFF CBCs quite well (6.4%, 4.3%, 1.8%, 3.2% and 2.9%, for types 1, 2, 3A, 3B and 4, respectively), and contacting ON CBCs more weakly (mostly CBC6 (2.0%) and CBC7 (1.4%), but not the XBC (0.2%)). The RBC, 38.3% of whose contact area is with the A2 cell, also strongly contacts (with 13.5%) ac34-84 (also known as an A17 amacrine cell)[31].

Even when two cell types strongly contact each other (Fig. 4b), the contact area between each individual pair of cells, one from each type, varies widely (Fig. 4a). To test whether individual cells still form reliable channels of information, we compared how the total contact area that a cell of type A makes with all cells of type B varies among the cells of type A. For example, the contact areas between individual ON SACs and all cells of the CBC5R 'type' (9.9% on average, the most strongly contacted one among the CBCs) vary by only about 16% (s.d./mean; Fig. 4c). At the same time, the contact area between A2 amacrine cells (ac52-90) and all RBCs, which is on average even stronger (24%), fluctuates more widely, by 25% (s.d./mean).

To test how much information about the actual synaptic connectivity is provided by our contact-area measurements, we used the size distributions for synaptic and incidental contacts, measured in a data set (k563, ref. 5) with prominently stained synaptic vesicles and thickenings (Fig. 3d, e and Supplementary Data 3a, b), to estimate, for all CBC–ganglion cell pairs, how many true synaptic contacts to expect for a given total contact area between two cells (Fig. 4d), and found that for a total contact area as small as 0.08 μm², at least one synaptic contact exists with a probability of 50%, increasing to 95% for an area of 1 μm².

Connectivity-based type classification

We next explored whether comprehensive contact information contained in the cell-to-cell matrix can be used to discriminate between otherwise very similar cell types. When we searched for a way to divide the CBC5s, which fall into two molecularly distinguishable classes in rats[32] and are too numerous for a single class in mouse[28], by using their connectivities to ganglion cells and amacrine cells, gc31-56 and gc36-51 emerged as potential discriminators (Fig. 5a). A reasonably complete tiling pattern resulted (Fig. 5b) when including only cells ($n = 22$) contacting gc31-56 more strongly than gc36-51 (the exception was a single cell, which was near that threshold but was not included to avoid strong axonal overlap; asterisk in Fig. 5a). This group of cells, 'CBC5A', also shows a strong repulsion between their dendritic centroids (Fig. 5c), indicating a mosaic and hence a pure type[33], and is specifically avoided by ac43-49 (Fig. 5a). The remaining 37 cells ('CBC5R') still show strong axonal overlap, lack a mosaic (Fig. 5b, c), and are thus probably a mixture of types for which we did not, however, find a connectivity-based discriminator. The depth profiles of CBC5A (first and third quartiles: 54% and 61%) and CBC5R (50% and 59%; Fig. 5d) seem to be different. Ten cells did not overlap the dendrites of both ganglion cell types (Fig. 5b) and were therefore collected into a separate group ('CBC5X').

XBC circuits

We next investigated how the XBC is integrated into the IPL circuitry (Fig. 6a–c). Like RBC and CBC7, XBC devotes less of its contact area to ganglion cells than the average bipolar cell (Fig. 6a). XBC strongly contacts (Supplementary Data 2b) medium/wide-field amacrine cells ac38-56 (15.5%) and ac53-59 (7.1%), of which ac53-59 shares the XBC sharp depth profile (Fig. 6b) and, in turn, makes contact with gc31-56 (3.5%) and gc47-57 (4.2%). Those ganglion cells, however, receive only minimal amounts (0.9% and 0.4%) of their contacts directly from the XBC, even though their dendrites strongly overlap XBC axons in depth (Fig. 6b). Instead gc31-56 receives direct bipolar cell contacts mainly from CBC5A (7.0%) and gc47-57 from CBC5R (12.0%). ac38-56 is bistratified, overlapping in the ON stratum with the XBC and in the OFF stratum with gc35-41 (Fig. 6b, c), which is clearly an OFF cell (contacting CBCs 3A, 3B and 4, with 5.4%, 6.3% and 5.4%, respectively; all other CBCs are at most 0.5%) and receives 10.0% of its contacts from ac38-56.

ON/OFF ganglion cell circuits

Some of the best studied ganglion cells respond to both ON and OFF stimuli. We therefore analysed the connection patterns onto several
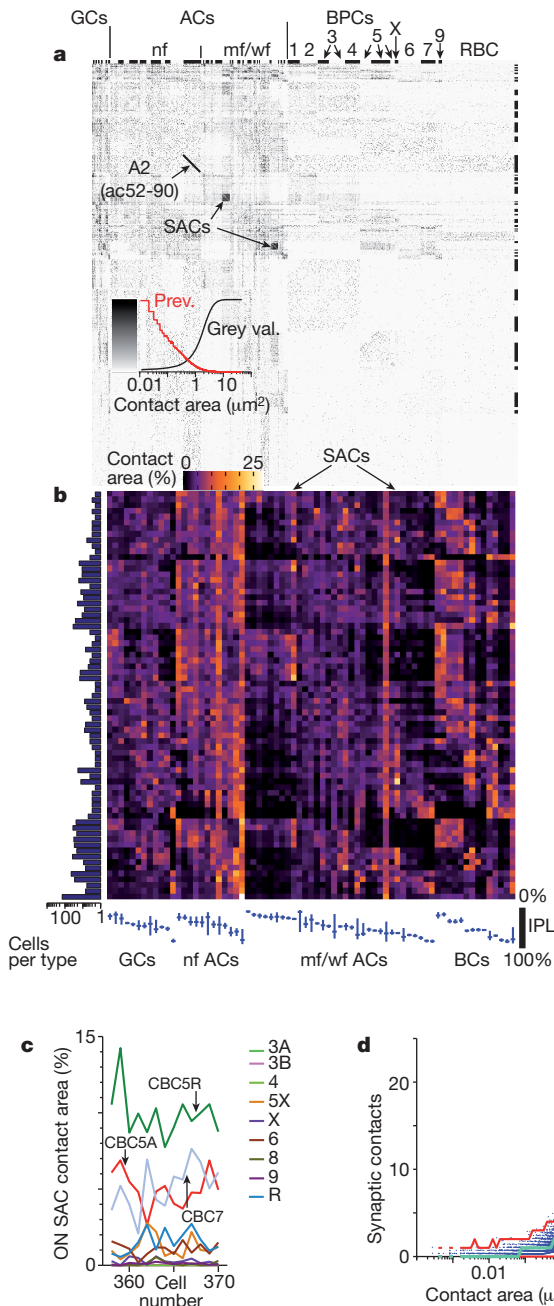
Figure 4 | Contact matrices. a, Cell–cell contact-size matrix (see also Supplementary Data 4 and 5). Classes: ganglion cells (GCs), amacrine cells (ACs), bipolar cells (BPCs), from left to right. Ordering within classes: ganglion cells, types by depth (average of first and third quartile) in the IPL. Amacrine cells: narrow-field (nf), medium/wide-field (mf/wf) (including displaced). Within sub-classes: by depth, except bipolar cells (by numbering in ref. 28, XBC after 5X, and RBC last). Within types: random order. Dark lines along top and right side: every other type. Inset (bottom left): contact area-to-grey value (grey val.) mapping and prevalence (prev.). **b**, Type–type matrix, normalized along rows; along left edge: cells/type (note log scale); along bottom edge: median and depth range (between quartiles) for each type. **c**, Total contact area between each ON SAC (ac60-65, cell numbers along the *x* axis) and, respectively, all CBCs and RBCs, normalized to the total contact area of each SAC. **d**, The number of true synaptic contacts expected (Stochastic simulation, 1,000 runs per cell pair) for each actual CBC-to-ganglion-cell pair using the fits in Fig. 3e versus the total cell–cell contact area (median: green line, lower and upper 95% confidence levels, red lines).

ganglion cells that ramify in both ON and OFF layers (Fig. 6d–f). Among those, gc36-51 ('W3a') and gc44-52 ('W3b') are consistent with cells labelled in the TYW3 mouse[34]. Either or both are likely to be
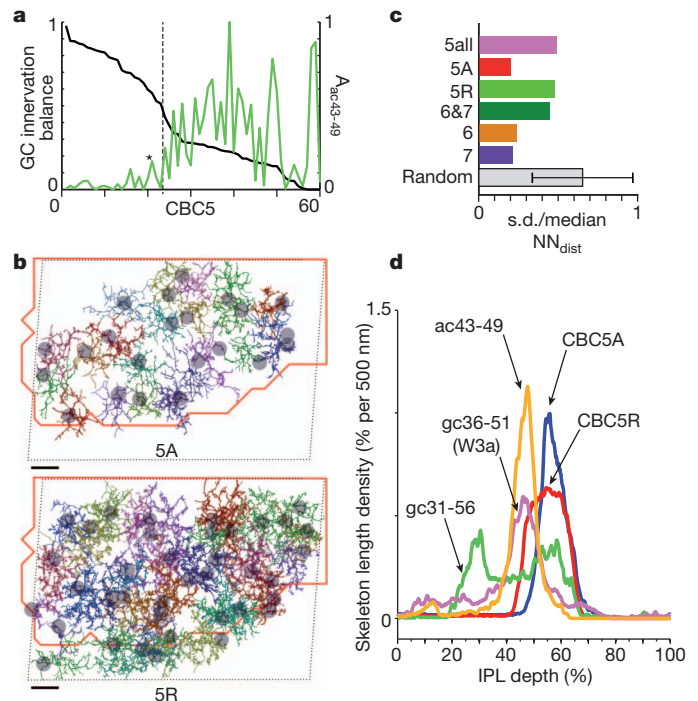
Figure 5 | CBC5 subtypes. a, CBC5s ordered by decreasing preference for gc31-56 over gc36-51 (black trace: contact area with all gc31-56s/sum of contact areas to gc31-56 and gc36-51). Also shown is the contact area with ac43-49 ($A_{ac43-49}$, green trace, relative to max). Dashed line denotes border between CBC5A and CBC5R. Asterisk denotes CBC5 cell switched to CBC5R to avoid mosaic violation. **b**, Light-axis views of CBC5A (5A; top) and CBC5R (5R; bottom) axons. Red outline: region containing dendrites from both gc36-51 and gc31-56; thin dashed line: data set border. Scale bars, 10 µm. **c**, Variation of dendritic–centroid nearest-neighbour distances (NN_{dist}) (standard deviation/median) for: all CBC5s, only 5A, only 5R, the mixture of 6 and 7, only 6, only 7, and a set of 1,000 simulations randomly placing 22 points (error bar denotes fifth to ninety-fifth percentile). **d**, Normalized skeleton density depth profiles.

homologous to what is called the 'local edge detector' in rabbit[35,36] (Fig. 6d). Their contact patterns with CBCs are mostly similar (gc36-51/gc44-52: CBC5R, 7.5%/11.5%; CBC5A, 1.3%/0.8%; CBC4, 3.0%/3.9%; CBC3A, 1.7%/1.8%; and CB3B, 3.2%/1.7%; Supplementary Data 1), with the exception of the outermost part of the inner nuclear layer (INL) (CBC2, 1.5%/0.1%, and CBC1, 1.6%/0.1%). Substantial contacts are made by gc36-51 and gc44-52 with several narrow-field amacrine cells, ac52-90 (6.0%/2.8% (ref. 37), A2), ac21-67 (3.8%/2.1%), ac51-70 (3.5%/5.0%) and ac21-44 (3.3%/2.2%). The strongest amacrine cell contact made by gc36-51 is with ac43-49 (6.8%), which straddles the boundary between ON and OFF layers (Supplementary Data 1), and also substantially contacts gc44-52 (5.6%) as well as ON and OFF bipolar cells (CBC5R, 9.3%, and CBC4, 5.0%). ac43-49 is one of two medium/wide-field amacrine cells that dedicate most of their contacts to gc36-51 and gc44-52 (Supplementary Data 1). The second is ac44-54 (7.0%/6.2%), a cell dominated by ON CBCs (7.9% with CBC5R compared to 1.3%, 2.0% and 1.2%, with CBCs 3A, 3B and 4, respectively).

The ON/OFF DSGC (gc30-63, Fig. 6f), as expected[5,21], strongly contacts SACs (9.2% and 11.4%, for ac25-31 (OFF SAC) and ac60-65 (ON SAC)), but substantial contacts from other medium/wide-field amacrine cells are conspicuously absent (ac34-84, 2.5%, all others < 1.6%). Like gc36-51/gc44-52 (W3a/b), the DSGC prefers CBC5R (6.9%) to CBC5A (1.9%, all other ON CBCs at most 1.1%). Its main OFF 'input' comes from CBC4 (3.2%) and CBC3 (A/B, 3.0%/2.7%). SACs make most contacts (Fig. 6e) among themselves (26.6% and 21.4% for ON and OFF). They discriminate less than the DSGC between CBC5R (9.7%) and CBC5A (5.0%), but, most notably, contact
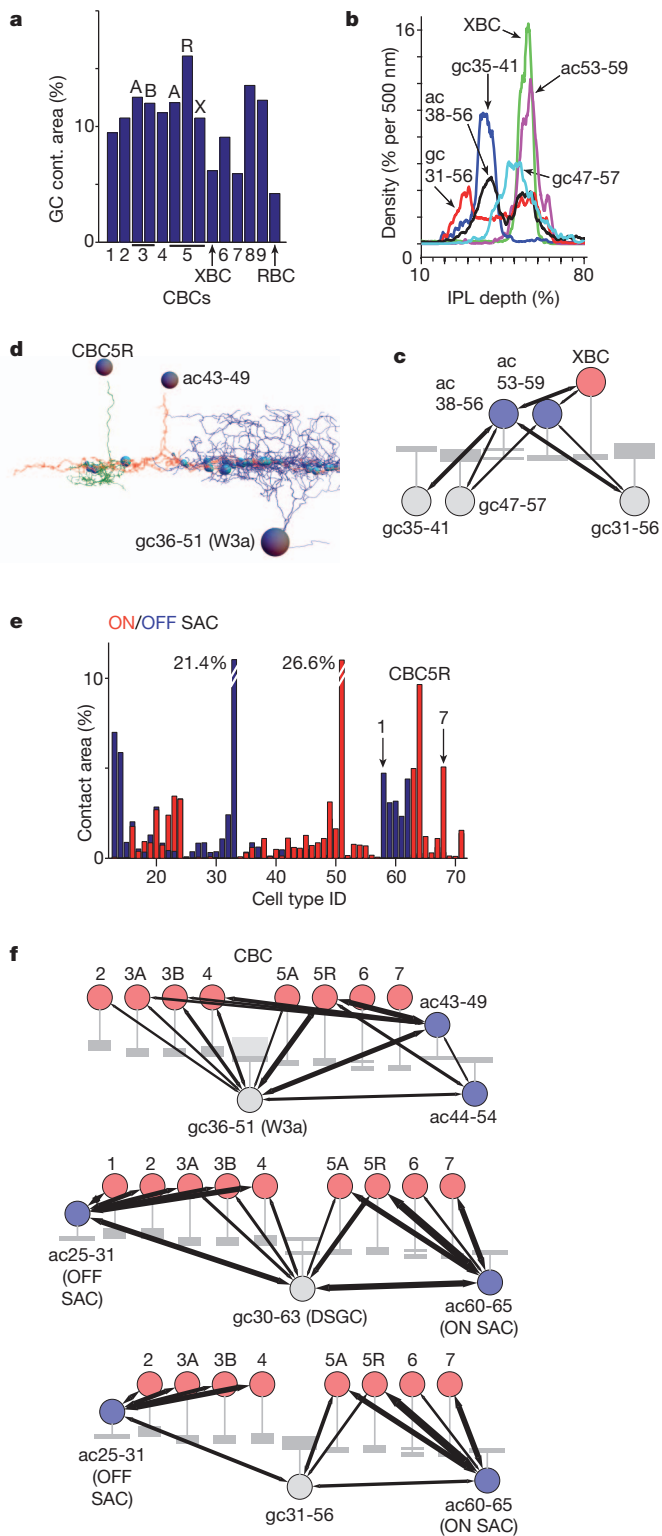
Figure 6 | Circuits originating from the XBC and ON/OFF cells. a–f, IPL circuitry from the XBC (**a–c**) and from three ON/OFF cells (**d–f**). **a**, Fractional contact areas between all ganglion cells and each bipolar cell. **b**, Depth profiles. **c**, XBC circuit schematic. **d**, One gc36-51/W3a (cell 16), one ac43-49 (cell 307), one CBC5R (cell 578) and all the detected contacts between (cyan spheres, volume proportional to contact area). **e**, Normalized contact areas for amacrine cells and bipolar cells with both SACs (ac25-31, blue; ac60-65, red). **f**, Circuit diagrams. Arrow width in circuit diagrams proportional to (total contact area between types)$^{0.5}$. Only connections with areas per type >30 μm² shown.

CBC7 (5.1%), which is largely ignored by the DSGC (1.1%, Fig. 6f). Similar differences are seen for the OFF sublamina: DSGC and SAC contact strengths to CBC1/CBC2 are 1.4%/0.5% and 4.7%/3.1%, respectively.

Our last example is the analysis of a cell not associated with any known type in mouse but possibly homologous to a rabbit retina[38] ON/OFF ganglion cell. gc31-56 is an ON/OFF cell by stratification (Fig. 2a, b), filling the space between the SAC bands (Fig. 2a, e), and 'connects' strongly to both SACs (ac60-65, 5.4%, and ac25-31, 7.1%). Surprising is the strong imbalance between ON and OFF bipolar cell 'input' (7.0%/3.7% for CBC5A/R, but only 0.8%, 0.7%, 0.9%, 1.5% and 1.2%, for CBC1, 2, 3A, 3B and 4).

Discussion

Our comprehensive analysis of the bipolar cells confirmed the existence of the ten bipolar cell types previously identified[28], and revealed the existence of the XBC, which had not emerged even in large genetic screens[39]. Although sharp stratification and large size (Fig. 1d, e and Supplementary Data 2a, also note the similarity to cluster 6 in ref. 40) suggest homology between the XBC and the giant bipolar cell described recently in the primate retina[41], the small size of the XBC dendrites relative to its axonal arbour argues against it. The functional role of the XBC is unclear. Its sparseness suggests low spatial resolution and its small dendritic fields suggest that it does not collect signals from all cells of one cone type, thus potentially forgoing some amount of signal. Curious is the absence of a bipolar cell with a similarly sharp stratification on the OFF side. Instead, we find an inter-layer connection via the symmetrically bistratified ac38-56 (Fig. 6b, c). One might speculate that the XBC is part of a luminance adaptation pathway.

Dense sampling and the complete high-resolution reconstruction of neurites, as is only possible with three-dimensional electron microscopy data, contributes in several ways to cell-type classification. First, when all cells of a class, for example, all bipolar cells, are reconstructed, no type will be missed and the prevalence of different types can be determined precisely (Fig. 1e, inset). Second, differences in neurite geometry can be compared for cells within the same piece of tissue. For almost all bipolar cells and a substantial fraction of ganglion and amacrine cells, it was thus possible to establish a correspondence to cell types described in the literature (Supplementary Data 7). We generally erred on the side of splitting groups and expect that some groups actually belong to the same type (for example, the similar connectivity to the XBC suggests that ac38-56 and ac37-52 could be the same type; Supplementary Data. 4). Third, even if they cannot be selectively stained and imaged, tiling and mosaic formation (both used to assess purity of type[33]) can be easily assessed (Figs 2b and 5b and Supplementary Data 1). Fourth, complete contact information can confirm or refine the definition of types (Fig. 5), and may ultimately become sufficient for classification all by itself[42].

Because of the constrained size of our data set, many amacrine cell and all ganglion cell neurites are truncated, and many larger neuron types are presumably completely missed[31,43]. Advances in volume electron microscopy technology[18] now make it possible to acquire volumes with a lateral extent of at least 500 μm. One might then, using the same tools and a similar manual annotation effort as were used in our study, densely reconstruct a central region of 100 μm in extent and trace neurites of passage far enough into the periphery to determine their cell type.

Although our analysis provides contact areas and not synaptic strength, the absence of contact always indicates a lack of synaptic connection. The absence of contacts between some cell types, for example, XBC and gc35-41 as well as CBC7 and DSGC, the neurites of which mingle extensively, confirms that Peters' rule[10] is routinely violated. Furthermore, it seems that large contacts are quite likely to be synaptic (at least between bipolar cells and ganglion cells; Figs 3e and 4d). Although we have not used them here, other geometric parameters describing contact shape might provide enough additional

information to identify actual contacts with near certainty for many types of synapses.

It has been our consistent experience that selectively enhancing cell-surface contrast[5] simplifies manual tracing and enables automatic volume segmentation. If recent results that suggest that even conventionally stained tissue can be reliably traced by hand (K.L.B. and M.H., unpublished observations) and automatically segmented[44] (M. Berning and M.H., personal communication) are confirmed it may no longer be necessary to trade traceability for synapse identification.

The reliability of the entries in the contact matrix depends on several factors. Likely dominant are neurite-continuity errors, which occur roughly six times per bipolar cell[25] but presumably mostly in the periphery and thus should cause only a small fractional loss (or false addition) of synapses. Local volume reconstruction seems to be fairly reliable. Finally, although not all contacts are synaptic, there are, typically, many contacts between any actually connected pair of cells[45,46], making it unlikely that any strong connection is spurious. The connectivity estimate between CBC5R (38 cells) and W3a (gc36-51, 3 cells), for example, is based on the areas of 1,358 observed contacts, for which our simulation predicts between 278 and 705 synaptic contacts (fifth and ninety-fifth percentiles, respectively) with a median of 483 contacts, that is, 13 per bipolar cell and 161 per ganglion cell. The direction of a potential synaptic connection can in most cases not be determined by visually inspecting the e2006 data set but contacts onto a ganglion cell, for example, are presumably never postsynaptic.

Our analysis of three ON/OFF layer cell types has several concrete functional implications, which, at the very least, will guide further exploration by other means. For example, 'bright' W3 cells (gc36-51 or gc44-52) respond much more vigorously to a small darkening spot than to a small brightening spot (Fig. 5b in ref. 47). This may well be due to the ac44-54-mediated feed-forward inhibitory pathway on the ON side (Fig. 6f and Supplementary Data 1), for which no corresponding pathways is seen on the OFF side. W3b–CBC contacts are concentrated on the ON side (ON/OFF: 15.2%/7.6%) but evenly balanced for W3a (10.9%/10.9%), which suggests that it is W3a (gc36-51) that corresponds to the physiologically examined cells described previously[47]. Another characteristic of the W3 cell is that its response is completely suppressed by movement in the receptive-field surround[48]. Given the lack of thin, unbranched processes emerging from its soma, it is unlikely that ac43-49 corresponds to the poly-axonal amacrine cell implicated in this suppression[48], but ac43-49 may well mediate (or at least augment) suppression for stimuli in the near-surround (M. Meister, personal communication). It could do this for OFF and for ON stimuli because it is contacted by CBCs in both OFF and ON layers (Fig. 6f and Supplementary Data 1).

In addition to DSGCs (gc30-63), SACs contact gc31-56 strongly (Fig. 6f). It will be interesting to find out whether gc31-56 is also direction sensitive, or at least motion sensitive, and why there is a morphological symmetry (Fig. 2b) between the ON and OFF layers in gc31-56 but a strong imbalance between the strong ON bipolar cell and the weak OFF bipolar cell 'input' (Fig. 6f).

The circuit motifs found for W3a/b, XBC and gc31-56 are only the first of many examples of motifs likely to be found when these data (a repository of raw data, skeletons and volume segmentation can be found at http://www.neuro.mpg.de/connectomics) are examined in the context of virtually every functional question in the retina.

METHODS SUMMARY

Tissue preparation for SBEM. The retinae for the e2006 and k563 data sets were prepared as described previously[5].

SBEM imaging and data analysis. The sample was mounted in a custom-built ultra-microtome operating inside the chamber of a field-emission scanning electron microscope (FEI QuantaFEG 200), and serial block-face imaged under 130 Pa hydrogen, at 3 keV landing energy, a dose of 14 electrons per nm^2, and a resolution of $16.5 \times 16.5 \times 25\ nm^3$ (for the conventionally stained sample, see Methods). A custom-designed back scattered-electron detector was used. SBEM data were aligned and stitched using custom Matlab routines. Skeletons were

manually traced by trained student annotators using custom written software (KNOSSOS, http://www.knossostool.org) and consolidated using RESCOP[25]. Volumes were traced using KLEE (M.H. et al., manuscript in preparation). Boundary classification was with a five-hidden-layer convolutional neural network that was trained using the MALIS procedure[49] (S.C.T. et al., manuscript in preparation). Segmentation used a 15-step iterative growth procedure, followed by a 6-step merging procedure. Data visualization was in KLEE, Knossos, Matlab, Mathematica and Amira.

Full Methods and any associated references are available in the online version of the paper.

1. White, J. G., Southgate, E., Thomson, J. N. & Brenner, S. The structure of the nervous system of the nematode *Caenorhabditis elegans. Phil. Trans. R. Soc. Lond. B* **314,** 1–340 (1986).
2. Varshney, L. R., Chen, B. L., Paniagua, E., Hall, D. H. & Chklovskii, D. B. Structural properties of the *Caenorhabditis elegans* neuronal network. *PLOS Comput. Biol.* **7,** e1001066 (2011).
3. Binzegger, T., Douglas, R. J. & Martin, K. A. C. A quantitative map of the circuit of cat primary visual cortex. *J. Neurosci.* **24,** 8441–8453 (2004).
4. Helmstaedter, M., de Kock, C. P., Feldmeyer, D., Bruno, R. M. & Sakmann, B. Reconstruction of an average cortical column *in silico. Brain Res. Rev.* **55,** 193–203 (2007).
5. Briggman, K. L., Helmstaedter, M. & Denk, W. Wiring specificity in the direction-selectivity circuit of the retina. *Nature* **471,** 183–188 (2011).
6. Stepanyants, A. & Chklovskii, D. B. Neurogeometry and potential synaptic connectivity. *Trends Neurosci.* **28,** 387–394 (2005).
7. Mishchenko, Y. et al. Ultrastructural analysis of hippocampal neuropil from the connectomics perspective. *Neuron* **67,** 1009–1020 (2010).
8. Hill, S. L., Wang, Y., Riachi, I., Schurmann, F. & Markram, H. Statistical connectivity provides a sufficient foundation for specific functional connectivity in neocortical neural microcircuits. *Proc. Natl Acad. Sci. USA* **109,** E2885–E2894 (2012).
9. Denk, W., Briggman, K. L. & Helmstaedter, M. Structural neurobiology: missing link to a mechanistic understanding of neural computation. *Nature Rev. Neurosci.* **13,** 351–358 (2012).
10. Peters, A. Thalamic input to the cerebral cortex. *Trends Neurosci.* **2,** 183–185 (1979).
11. Markram, H., Lubke, J., Frotscher, M., Roth, A. & Sakmann, B. Physiology and anatomy of synaptic connections between thick tufted pyramidal neurones in the developing rat neocortex. *J. Physiol. (Lond.)* **500,** 409–440 (1997).
12. Fried, S. I., Munch, T. A. & Werblin, F. S. Mechanisms and circuitry underlying directional selectivity in the retina. *Nature* **420,** 411–414 (2002).
13. Asari, H. & Meister, M. Divergence of visual channels in the inner retina. *Nature Neurosci.* **15,** 1581–1589 (2012).
14. Stevens, J. K., Davis, T. L., Friedman, N. & Sterling, P. A systematic approach to reconstructing microcircuitry by electron microscopy of serial sections. *Brain Res.* **2,** 265–293 (1980).
15. Sterling, P. Microcircuitry of the cat retina. *Annu. Rev. Neurosci.* **6,** 149–185 (1983).
16. Famiglietti, E. V. Synaptic organization of starburst amacrine cells in rabbit retina: analysis of serial thin sections by electron microscopy and graphic reconstruction. *J. Comp. Neurol.* **309,** 40–70 (1991).
17. McGuire, B. A., Stevens, J. K. & Sterling, P. Microcircuitry of bipolar cells in cat retina. *J. Neurosci.* **4,** 2920–2938 (1984).
18. Briggman, K. L. & Bock, D. D. Volume electron microscopy for neuronal circuit reconstruction. *Curr. Opin. Neurobiol.* **22,** 154–161 (2012).
19. Masland, R. H. The neuronal organization of the retina. *Neuron* **76,** 266–280 (2012).
20. Vaney, D. I., Sivyer, B. & Taylor, W. R. Direction selectivity in the retina: symmetry and asymmetry in structure and function. *Nature Rev. Neurosci.* **13,** 194–208 (2012).
21. Euler, T., Detwiler, P. B. & Denk, W. Directionally selective calcium signals in dendrites of starburst amacrine cells. *Nature* **418,** 845–852 (2002).
22. Zhou, Z. J. & Lee, S. Synaptic physiology of direction selectivity in the retina. *J. Physiol. (Lond.)* **586,** 4371–4376 (2008).
23. Wei, W., Hamby, A. M., Zhou, K. & Feller, M. B. Development of asymmetric inhibition underlying direction selectivity in the retina. *Nature* **469,** 402–406 (2011).
24. Denk, W. & Horstmann, H. Serial block-face scanning electron microscopy to reconstruct three-dimensional tissue nanostructure. *PLoS Biol.* **2,** e329 (2004).
25. Helmstaedter, M., Briggman, K. L. & Denk, W. High-accuracy neurite reconstruction for high-throughput neuroanatomy. *Nature Neurosci.* **14,** 1081–1088 (2011).
26. Jain, V. et al. Supervised learning of image restoration with convolutional networks. *IEEE 11th International Conference on Computer Vision* **2,** 1–8 (2007).
27. Turaga, S. C. et al. Convolutional networks can learn to generate affinity graphs for image segmentation. *Neural Comput.* **22,** 511–538 (2010).
28. Wässle, H., Puller, C., Muller, F. & Haverkamp, S. Cone contacts, mosaics, and territories of bipolar cells in the mouse retina. *J. Neurosci.* **29,** 106–117 (2009).
29. Amthor, F. R., Oyster, C. W. & Takahashi, E. S. Morphology of on-off direction-selective ganglion cells in the rabbit retina. *Brain Res.* **298,** 187–190 (1984).
30. Strettoi, E., Raviola, E. & Dacheux, R. F. Synaptic connections of the narrow-field, bistratified rod amacrine cell (AII) in the rabbit retina. *J. Comp. Neurol.* **325,** 152–168 (1992).

31. Macneil, M. A., Heussy, J. K., Dacheux, R. F., Raviola, E. & Masland, R. H. The shapes and numbers of amacrine cells: matching of photofilled with Golgi-stained cells in the rabbit retina and comparison with other mammalian species. *J. Comp. Neurol.* **413,** 305–326 (1999).

32. Fyk-Kolodziej, B. & Pourcho, R. G. Differential distribution of hyperpolarization-activated and cyclic nucleotide-gated channels in cone bipolar cells of the rat retina. *J. Comp. Neurol.* **501,** 891–903 (2007).

33. Wassle, H. & Riemann, H. J. Mosaic of nerve-cells in mammalian retina. *Proc. R. Soc. Lond. B* **200,** 441–461 (1978).

34. Kim, I. J., Zhang, Y., Meister, M. & Sanes, J. R. Laminar restriction of retinal ganglion cell dendrites and axons: subtype-specific developmental patterns revealed with transgenic markers. *J. Neurosci.* **30,** 1452–1462 (2010).

35. Levick, W. R. Receptive fields and trigger features of ganglion cells in the visual streak of the rabbits retina. *J. Physiol. (Lond.)* **188,** 285–307 (1967).

36. Amthor, F. R., Takahashi, E. S. & Oyster, C. W. Morphologies of rabbit retinal ganglion cells with complex receptive fields. *J. Comp. Neurol.* **280,** 97–121 (1989).

37. Kolb, H., Nelson, R. & Mariani, A. Amacrine cells, bipolar cells and ganglion cells of the cat retina: a Golgi study. *Vision Res.* **21,** 1081–1114 (1981).

38. Sivyer, B., Venkataramani, S., Taylor, W. R. & Vaney, D. I. A novel type of complex ganglion cell in rabbit retina. *J. Comp. Neurol.* **519,** 3128–3138 (2011).

39. Siegert, S. *et al.* Genetic address book for retinal cell types. *Nature Neurosci.* **12,** 1197–1204 (2009).

40. Badea, T. C. & Nathans, J. Quantitative analysis of neuronal morphologies in the mouse retina visualized by using a genetically directed reporter. *J. Comp. Neurol.* **480,** 331–351 (2004).

41. Joo, H. R., Peterson, B. B., Haun, T. J. & Dacey, D. M. Characterization of a novel large-field cone bipolar cell type in the primate retina: evidence for selective cone connections. *Vis. Neurosci.* **28,** 29–37 (2011).

42. Seung, H. S. Reading the book of memory: sparse sampling versus dense mapping of connectomes. *Neuron* **62,** 17–29 (2009).

43. Masland, R. H. The fundamental plan of the retina. *Nature Neurosci.* **4,** 877–886 (2001).

44. Andres, B. *et al.* in *Computer Vision – ECCV 2012 Lecture Notes in Computer Science* (eds Fitzgibbon, A. *et al.*) 778–791 (Springer, 2012).

45. Tsukamoto, Y., Morigiwa, K., Ueda, M. & Sterling, P. Microcircuits for night vision in mouse retina. *J. Neurosci.* **21,** 8616–8623 (2001).

46. Calkins, D. J. & Sterling, P. Microcircuitry for two types of achromatic ganglion cell in primate fovea. *J. Neurosci.* **27,** 2646–2653 (2007).

47. Zhang, Y., Kim, I. J., Sanes, J. R. & Meister, M. The most numerous ganglion cell type of the mouse retina is a selective feature detector. *Proc. Natl Acad. Sci. USA* **109,** E2391–E2398 (2012).

48. Ölveczky, B. P., Baccus, S. A. & Meister, M. Segregation of object and background motion in the retina. *Nature* **423,** 401–408 (2003).

49. Turaga, S. C., Briggman, K., Helmstaedter, M., Denk, W. & Seung, H. S. Maximin affinity learning of image segmentation. *Adv. Neural Info. Proc. Syst.* **22,** 1–8 (2009).

Supplementary Information is available in the online version of the paper.

METHODS

Data acquisition. A retina from a 30-day old-C57BL/6 mouse (data set e2006) was prepared to selectively enhance cell outlines by using the horseradish peroxidase (HRP)-mediated precipitation of 3,3'-diaminobenzidine (DAB), as described previously[5], and stained with osmium and lead citrate. The shrinkage of our tissue was very likely the same as that for the e2198 sample[5], which was imaged in the living state by two-photon microscopy and then by SBEM, allowing a precise estimate (14%) of the linear shrinkage factor (K.L.B. *et al.*, unpublished observations). All procedures were approved by the local animal care committee and were in accordance with the law of animal experimentation issued by the German Federal Government.

The embedded tissue was trimmed to a block face of ~200 μm × 300 μm and imaged in a scanning electron microscope with a field-emission cathode (QuantaFEG 200, FEI Company) and a custom-designed back scattered-electron detector based on a silicon diode (AXUV, International Radiation Detectors) combined with a custom-built current amplifier (J. Tritthardt, Max Planck Institute for Medical Research, electronics shop). The incident-electron energy was 3.0 keV, the beam current ~100 pA. At a pixel dwell time of 6 μs and a pixel size of 16.5 nm × 16.5 nm this resulted in an electron dose of about 14 electrons nm^{-2}, not accounting for skirting due to low-vacuum operation. The chamber was kept at a pressure of 130 Pa hydrogen to prevent charging. The electron microscope was equipped with a custom-made microtome[24], which allows the repeated removal of the block surface at a cutting thickness of ≥25 nm. A total of 3,200 consecutive slices were imaged, leading to a data volume of 8,192 × 7,072 × 3,200 voxels (a 4 × 4 mosaic of images 2,048 × 1,768 pixels in size). As the edges of neighbouring mosaic images overlapped by ~1 μm, this corresponds to a physical size of about 132 μm × 114 μm for each slice and a total thickness of 80 μm. Note that stitching led to substantial shear (about 4 degrees) in *z*.

The cutting speed was 0.5 mm s^{-1}. To avoid chatter and ensure even cutting, the diamond knife (facet angle 50°, clearance angle 20°, Diatome) was vibrated along the knife-edge direction with a frequency of ~12 kHz using a small piezo actuator integrated into the knife holder[50]. Focus and astigmatism were continually monitored (using the 'heuristic algorithm' described previously[51]) on the basis of acquired images and automatically adjusted. After each cut, a low-resolution overview image was acquired and used to automatically detect cutting debris on the surface. If debris was detected, the knife was passed over the surface with 40-nm clearance in an attempt to remove the debris. Consecutive slices were aligned offline to sub-pixel precision by Fourier shift-based interpolation, using cross-correlation-derived shift vectors. Note that the sub-volume inside the data set that contains valid data is a rhomboid.

Skeletonization. The data set was prepared as described previously[25] for crowd-sourced skeletonization by trained human annotators, which were specifically recruited from the local student population. This is different from some other 'citizen science' projects but encountered similar problems, such as the need to establish a mechanism for cross-validation. The data were visualized and annotations were captured using the KNOSSOS program[25] (http://www.knossostool.org). First, all somata in the inner plexiform and ganglion cell layers were identified and classified as ganglion, amacrine, bipolar, horizontal and glia cells, using the location of each soma and the types of neurites emerging from it. Then, starting from the soma, each neuron was traced, by multiple tracers (6, 4 and 4 for ganglion cells, bipolar cells and amacrine cells, respectively). Tracings were then consolidated using RESCOP[25] with the following refinements: all edges within 3 μm of the soma centre were eliminated, no edges were eliminated between 3 and 10 μm, and, except for somata in the ganglion cell layer, branches were allowed to pass 15 μm only if their multiplicity (pro votes) compared to the maximum multiplicity of any branch leaving the same soma (total votes) was acceptable according to the voting rules[25]. Type-grouped skeletons were visually scanned using Amira (VSG, Merignac Cedec) and KNOSSOS. For 34 apparently aberrant branches, their originating branch points were inspected in the raw data, and removed if erroneous (12 cases). Density profiles were calculated by collecting the edge centres into 50-nm-wide bins using the length divided by the total vote count[25] for each edge as the weight. Histograms were normalized and used to calculate the quartiles.

Type classification. Cells were visually inspected using views as shown in Fig. 1b. The morphological criteria used were the neurite density with depth in the IPL and the lateral branching pattern. Connectivity information was used to subdivide CBC5s (see below). If a cell could not be grouped with at least one other cell it was not assigned to a type and instead added to the 'orphan' category, even when showing a discernible neurite morphology (Supplementary Data 6). The contact data for the 110 orphan cells are not shown in Fig. 4 but are included in Supplementary Data 4 and 5. We refer to the types here by their column/row index in the type matrix. Supplementary Data 4, sheet 3, and Supplementary Data 7

provide translation between, respectively, the different indices for individual cells and between type indices, type identifiers, and common type names.

The classification of the cells proceeded as follows. The neurite ramification pattern in the IPL, particularly its distribution along the light axis and its overall lateral size, was used first. We don't usually comment when cells obviously cluster into a type by those criteria (for example, types 9, 33 and 51). Unless otherwise indicated, percentage numbers represent position along the light axis. As the boundaries of the IPL (0%, 100%), we defined the points where the total skeleton density falls below 15% of its maximum. We use the point where the skeleton densities of ON and OFF bipolar cells cross over (46.5%), as the ON/OFF boundary. In some cases (types 58–62, corresponding to CBC1–4, and in one case for the CBC5A versus CBC5R distinction) we used, in addition, tiling (the lateral overlap between neurites in the plane of the retina).

First, we identified the ON and OFF SACs (types 33 and 51). We next considered all remaining cells that had their somata in the GCL. Because we were initially not sure how reliably the axon could be detected, we did not use the presence of an axon as a criterion to distinguish ganglion cells from displaced amacrine cells. In all but one of the cells classified as ganglion cells an axon was found eventually. We begin with the actual ganglion cells (types 1–12), postponing the discussion of displaced amacrine cells (types 27, 43, 51 and 56–57).

There are three clearly bistratified ganglion cell types (2, 8 and 9) that extensively ramify in both ON and OFF layers. Only type 2 has one of its bands immediately adjacent to the INL, whereas the lowest band of type 8 is well separated from the INL. Additional discrimination was provided by bands at 50% and 70% for types 2 and 8, respectively. Only one of the type-8 cells shows all aspects of the dendritic tree, whereas the other two cells are presumably missing parts of the dendrite inside the reconstructed volume but share enough features to put them into the same class. Type 9 is the ON/OFF DSGC.

Type 6 could be called bistratified but the space between the bands still contains a lot of neurite. The two bands are just inside the choline acetyltransferase (ChAT) bands, which is where the SACs (types 33 and 51) and DSGCs (type 9) ramify. Types 7 and 10 both have only one band straddling the ON/OFF border, but 7 has numerous branches going all the way to the INL. Types 7 and 10 probably correspond to the two subtypes labelled in the TYW3 mouse[34].

Next we considered cells that ramify mostly in the OFF (types 1, 3, 4 and 5) or the ON layer (types 11 and 12). Among those, only types 1 and 3 ramify all the way up to the INL (a slight dendritic resemblance to type 27, a displaced amacrine cell, can be resolved by looking at the lateral (in-plane) branching pattern, which is much more tortuous for 27). Type 1 has multiple branches emerging directly from the soma but type 3 only has a single one. Type 5 has a much denser in-plane branching pattern than type 4. Type 11 ramifies further towards the GCL than type 5 and is broader than type 10. Type 12 is the only ganglion cell ramifying in a single band adjacent to the GCL.

Among the amacrine cells we started with the narrow-field types (13–24). Types 18, 20 and 24 all reach deep into the ON layer and have bands in both the ON and OFF layers, which was used to separate them from 23 and 22, with no bands in the OFF layer, even though the variability of the OFF band in type 20 made it difficult to distinguish type 20 and 22 cells, possibly causing some misclassification. Type 18 shows a sharp band at about 70% and a broader band touching the INL. Types 13 and 14 were difficult to distinguish, but 14 has a clearer gap to the INL and a less dense dendrite. Types 16 and 17 differ in lateral size. Some overlap between 16 and 15 cannot be completely ruled out but most type 15 cells are shorter and end mostly in a dense band. Types 19 and 21 differ in lateral size (21 and 42 may be the same type).

Next we considered cells (types 25, 28, 30–32, 37, 39, 41, 47, 53 and 57) in which the branching pattern suggested wide fields, for example, because only few of their branches ended inside the sample. Many of these cells (types 25, 37, 39, 41, 47 and 53) show a sharp lamination in depth. Only type 25 ramifies close to the INL. Type 30 is more strongly branched than 28 and ramifies broadly in depth, unusual for wide-field cells. Type 28, unlike type 30, has two branches leaving in opposite directions. Type 31 dendrites, uniquely among the cells reconstructed, go off into a narrow segment. Type 32 ramifies in the OFF ChAT band, but branches differently from the OFF SAC (type 33). Type 39 has only a single primary branch, whereas type 41, which stratifies at almost the same depth, has several. Note that types 37, 41/39 and 47 subdivide the space between the ChAT bands into three equal sublaminae.

The remaining amacrine cells are medium-field cells (types 26, 27, 29, 33–36, 38, 40, 42–46, 48–52 and 54–57), including the unmistakable SACs (types 33 and 51, see above). Types 34 (an interplexiform cell), 49 and 52 uniquely reach all the way across the IPL. Type 49 has the very distinctive 'waterfall' anatomy and type 52 lacks the sharp band right outside the INL of type 34. Types 35 and 38 were distinguished by how far their dendrites reached towards the GCL. Types 48 and

50 differ in primary dendrite shape and in-plane size but may still be the same type. Type 45 has more primary dendrites than type 54.

To classify bipolar cells (types 58–71) we first tried to establish similarity to the types described previously[28]. The correspondence was mostly obvious for RBCs (type 71) and ON CBCs (types 63-70)—see the main text for CBC5 (types 63–65) and XBC (type 66)—but rather difficult for OFF CBCs (types 58–62).

First, all OFF bipolar cells were sorted using the seventy-fifth percentile of the cumulative skeleton density in depth (starting from 0%) then, the lower 58.2% (their prevalence; see Table 1 in ref. 28) of cells were placed in the CBC3A/3B/4 and the remainder into the CBC1/2 category. The former was then sorted by the twenty-fifth percentile. Because this distribution was not clearly separable (consistent with the CBC4 width being smaller and more variable than drawn previously[28]), we began to collect the CBC4 cells starting at the highest twenty-fifth percentile numbers, adding cells consistent with the mosaic until the required prevalence was reached. The same procedure, now using the axonal coverage area, was used to separate CBC3A from B, reported to be larger CBC3A (ref. 28) and CBC1/2 using the spread in depth of the axon (twentieth to eightieth percentile). Finally, all mosaics were inspected again, six cells were reassigned, and one cell (cell 927, Supplementary Data 6) was moved to the 'orphan' group as it did not fit into any of the mosaics. In the resulting grouping, types 60–62 show a ramification-free zone adjacent to the INL that is lacking in types 58 and 59. Type 59 dendrites, if anything, are closer to the INL than type 58 dendrites. Type 62 ramifies slightly more widely in depth than types 60 and 61. Type 61 tends to be smaller than type 60.

Segmentation. A feed-forward convolutional neural network[27] was trained to classify connectedness (roughly a probability) between voxels sharing a face (the Matlab code and the network weights are in Supplementary Data 8). Several sub-volumes (each $100 \times 100 \times 100$ voxels in size) were fully segmented using KLEE and served as the initial training data, which was gradually augmented by semi-automatically segmented volumes (proofread segmentations generated with earlier network versions), yielding a final training set of 12 substantial volumes ranging from $(128 \text{ voxels})^3$ to $(240 \text{ voxels})^3$ (more than 800 million example image patches, including translations and rotations). The network contained 5 hidden layers with 10 feature maps each and was trained for over 5.5 million mini-batch gradient update steps until convergence, corresponding to many central processing unit (CPU) months, in a greedy and supervised layer-wise manner using a modified version of MALIS[49], modified to assign equal weight to each segment (S.C.T. *et al.*, manuscript in preparation). All filters were $7 \times 7 \times 7$ voxels in size and used a logistic sigmoid nonlinearity. After classifying voxel connectedness for the whole data set, segmentation was as follows. First, the voxels were clustered using a threshold of 0.9999. Clusters with ≥10 voxels were used as seeds and grown to threshold of 0.999. Unconsumed voxels were clustered using the same threshold, followed by seed selection and growth, now to 0.99. This procedure was repeated using thresholds of 0.98, 0.96, 0.94, 0.92, 0.9, 0.85, 0.8, 0.7, 0.6, 0.5, 0.4 and 0.2, and resulted in the assignment of each voxels in the data set to a supervoxel (on average 517 voxels), which were now merged using the following criteria: first, objects larger than 36 voxels were merged with each other if the boundary classifier averaged across their interface was above a threshold that was gradually lowered from 0.95 to 0.75 in linear steps of 0.05. In the next phase, only objects of unequal size were allowed to merge. The 'forbidden' size intervals (in voxels) and the interface thresholds for each step were: 2,000–200, 0.65; 2,000–200, 0.6; 2,000–200, 0.55; 2,000–200, 0.55; 2,000–400, 0.6; 2,000–800, 0.6; 2,000–1,600, 0.6; 2,000–1,600, 0.6; 2,000–1,600, 0.6; 5,000–2,000, 0.6; 10,000–3,000, 0.6; 20,000–4,000, 0.6; 25,000–5,000, 0.6; 30,000–6,000, 0.6.

This increased the average segment size to 2,443 voxels. Segments were then assigned to that skeleton that had the most nodes in the segment (only a small fraction contained nodes from more than one skeleton). All segments assigned to a skeleton comprise the volume reconstruction of the corresponding cell. The volume fraction erroneously assigned was estimated by summing the volume of all segments that contained multiple skeletons, weighted by the fraction of minority nodes in the segment and divided by the total volume of segments assigned to any skeleton.

Contact detection. To quantify contacts between segments, segment-to-segment overlap matrices were calculated between the original segmentation and versions shifted by one voxel, respectively, in the x, y and z directions. The resulting three collections of overlapping voxels were combined and classified and grouped into 'contacts' (Supplementary Data 8) using a dilation-based proximity measure. The contact areas were calculated using the following weights (nm^2) depending on according to the combination of direction sets they occurred in: 412.5 (x or y), 272.25 (z), 583.3631 (x and y), 494.2432 ((x or y) and z), 643.7644 (x, y and z). This corrects for the anisotropy in voxel size and to some extent for the error introduced by the angle of the contact surface. For surfaces perpendicular to one of the principal axes, the face diagonals, or the space diagonal this estimate is exact.

Error estimation. To probe the frequency of missed contacts (false negatives) we selected 100 random locations on one skeleton (cell 17, gc36-51, W3) and searched for true contacts with an, according to the cell–cell matrix, highly connected cell (cell 344, ac34-84). All 16 true contacts found were also found by the automated detection routine. To estimate the false positive rate we randomly selected 20 of the 7,217 contacts that the same ganglion cell made with other cells and visually inspected the corresponding locations in the raw data. In one case no actual contact existed (a piece of debris was erroneously attributed by the segmentation routine to cell 344).

Sizes for synaptic and non-synaptic contacts. Synaptic and non-synaptic contacts in the conventionally stained data set (k563) were selected and their contact area determined in one of two ways. (1) Starting from a bipolar cell axon terminal, a synaptic ribbon was located (Fig. 3d), the two postsynaptic dyadic partners were found and their class determined, using the presence or absence of synaptic vesicles (found in amacrine but not ganglion cell dendrites). All three dyadic partners and, in addition, a nearby non-synaptic contact were manually reconstructed using the KLEE software tool (M.H. *et al.*, manuscript in preparation) in a region including all three contacts. The contact areas were determined as follows. Surface triangulations were generated for each volume reconstruction, then for each triangle it was determined whether there was another object within 144 nm above it, next the contact area with this object was calculated as the sum over all hits in that object weighted by the triangle areas. (2) All contacts with bipolar cells were reconstructed on several pieces of ganglion cell dendrite, quantified, and classified as synaptic when a ribbon was present and non-synaptic otherwise. Classification, segmentation and contact detection were performed independently for each member of a set of overlapping cubes (257 voxels on a side), one cube for each interior data cube (128 voxels on a side). Each of those cubes overlaps one data cube completely and 26 cubes partially. To avoid double counting, we counted a contact only when the largest part of the contact was inside the completely overlapped (central) data cube.

50. Studer, D. & Gnaegi, H. Minimal compression of ultrathin sections with use of an oscillating diamond knife. *J. Microsc.* **197,** 94–100 (2000).
51. Binding, J., Mikula, S. & Denk, W. Low-dosage maximum-*a-posteriori* focusing and stigmation. *Microsc. Microanal.* **19,** 38–55 (2013).